Available online at www.sciencedirect.com
ScienceDirect
Journal of Power Sources 176 (2008) 54–61
JOURNAL OF POWER SOURCES
www.elsevier.com/locate/jpowsour

Evaluation of Laves-phase forming Fe–Cr alloy for SOFC interconnects in reducing atmosphere☆

Teruhisa Horita*, Haruo Kishimoto, Katsuhiko Yamaji, Yueping Xiong, Natsuko Sakai, Manuel E. Brito, Harumi Yokokawa

National Institute of Advanced Industrial Science and Technology (AIST), AIST Central 5, Higashi 1-1-1, Tsukuba 305-8565, Japan

Received 19 September 2007; received in revised form 12 October 2007; accepted 13 October 2007
Available online 23 October 2007

Abstract

A Laves-phase forming Fe–Cr alloy was evaluated as interconnects for solid oxide fuel cells (SOFCs) in reducing atmosphere (in H_2-H_2O). The oxide scale growth was compared between Laves-phase forming alloy and typical stainless steel (SUS430). The oxide scale growth rates were decreased in the Laves-phase forming alloy, and the area-specific resistance (ASR) of oxidized Laves-phase forming alloy showed the lower values than that of SUS430. The temperature dependence of 1/ASR for the oxidized alloy was different between Laves-phase forming alloy and SUS430. The oxygen diffusivity in the oxide scale was also evaluated by the stable isotope oxygen ($^{18}O_2$) diffusion in the scale. The chemical diffusion coefficients of isotope oxygen in the oxide scale showed the smaller value for the Laves-phase forming alloy ($D = 7.0 \times 10^{-13}$ cm^2 s^{-1}) than that for SUS430 ($D = 4.6 \times 10^{-12}$ cm^2 s^{-1}) at 1073 K. A relatively high diffusivity of oxygen was estimated in the Mn–Cr spinel oxide on the top surface of oxide scales. Inward diffusion of oxygen and outward diffusion of cation in the oxide scale were discussed to consider the oxide scale growth mechanism.

Keywords: Fe–Cr alloy; Interconnect; Solid oxide fuel cells (SOFCs); Oxide scale; Grain boundary

1. Introduction

In the intermediate operation temperature (773–1073 K) solid oxide fuel cells (SOFCs), alloys have been considered as promising materials for interconnects [1,2]. Alloys are excellent materials in terms of mechanical strength and gas-tightness. However, during operating condition (above 773 K and air/fuel stream), protective oxide scale is formed on the alloy surface. This oxide scale is effective to prevent further oxidation of alloy and to reduce the vapor pressure of Cr from Fe–Cr alloy. When the alloys contain the amounts of Cr more than 18 mass%, the protective oxide scale will be Cr_2O_3-based oxides on the alloy surface. Also, an addition of Mn is effective to form Cr–Mn spinel top surface of oxide scale, which further reduces the Cr vapor pressures and increase the electrical conductivity of oxide scales. Thus, the compositional modification of Fe–Cr alloy is important to have a stable oxide scale composition and structures.

So far, several kinds of candidate Fe–Cr alloys have been proposed by many authors, and some Fe–Cr alloys showed a relatively high resistance against oxidation [3–7]. We investigated the oxide scale formation mechanism on several candidate Fe–Cr alloys, especially in reducing atmospheres (in H_2-H_2O or CH_4-H_2O fuels) [8–10]. In our previous study, the oxide scale formation was found to occur from the alloy grain boundaries with forming the ridges of Mn and Fe high concentration. This suggests that the alloy grain boundaries are fast diffusion paths for supplying the elements to the oxide scale. A fast transport of elements at the grain boundaries can affect the oxide scale formation rates and oxide scale structures. In recent years, a new strategy has been proposed to control the cation diffusivity at the alloy grain boundaries: an addition of Nb and Mo into Fe–Cr alloy is effective to control the cation diffusivity at the alloy grain boundaries by forming Laves-type phases (such as Fe_2Nb) in air atmosphere [11–13]. The formed oxide scales are thin and compact, which is expected to be suitable for SOFC

☆ This paper was presented at the 2nd Symposium on Fuel Cells Science, Technology: Bridging Processing and Performance (FCST) Materials Processing, Properties and Performance (MP3) at Beijing, China on September 2007.

* Corresponding author. Tel.: +81 29 861 9362; fax: +81 29 861 4540.
E-mail address: t.horita@aist.go.jp (T. Horita).

0378-7753/$ – see front matter © 2007 Elsevier B.V. All rights reserved.
doi:10.1016/j.jpowsour.2007.10.041

interconnect. However, when considering SOFC application, there is no information available for the oxide scale formation and growth in H_2-H_2O atmosphere. Also, no information is available for electrical conductivity and oxygen diffusivity of oxidized alloys. The purpose of this study is to clarify the elemental distribution of oxide scales formed in H_2-H_2O, and to clarify the electrical properties and oxygen diffusivity in the oxide scales for the Laves-phase forming alloys. The application of Laves-phase forming alloys for SOFC interconnects is discussed.

2. Experimental

2.1. Materials

The examined samples were Fe–Cr alloys (ferritic alloys) with Cr concentration of 18–20 mass%. To clarify the effect of alloy grain boundaries on the oxide scale formation, two different kinds of Fe–Cr alloys have been compared: Laves-phase forming Fe–Cr alloy and typical stainless steel (SUS430). The chemical compositions of these alloys are listed in Table 1. The surface of the alloys was polished by a diamond paste up to 1/4 μm in diameter to obtain a flat and mirror surface. The oxidation experiments were conducted in H_2-H_2O atmosphere at 1073 K. The hydrogen and water vapor pressures were $p(H_2) = 1.8$ kPa and $p(H_2O) = 11$ kPa with Ar dilution at a flow rate of 50 ml min^{-1} to simulate SOFC fuel gas. The calculated oxygen partial pressure was $p(O_2) = 1.5 \times 10^{-12}$ Pa ($\approx 1.5 \times 10^{-17}$ bar) when the equilibrium was attained by the mixture gases. The oxide scale was formed on the alloys surface by reacting with H_2O in H_2-H_2O.

2.2. Analysis of oxide scales

The surface microstructures and depth profiles of oxide scales were analyzed by several kinds of analytical methods. The oxide scale phases formed were determined by X-ray diffraction (XRD, Phillips, PW-1800). The microstructures of surface and at the oxide scale/alloy interfaces were analyzed by scanning electron microscope (SEM, Keyence VE7800) with energy dispersive X-ray spectroscopy (EDX, Kevex). The depth profiles of major and minor elements around the oxide scale/alloy interfaces were examined by glow discharge optical emission spectroscopy (GDOES, Jobin Yvon/ Horiba, JY-5000RF). The thickness of oxide scales were estimated from SEM images of cross-section or the depth profiles of O-signals of GDOES. The area-specific resistance (ASR) after forming oxide scales was measured by 4-probe AC impedance methods with amplitude of 1 mA. The platinum paste was applied on the oxide scale surface with an area of 1 cm^2. The impedance spectra show only ohmic resistance corresponding to the resistance both from oxide scale and alloy. The oxygen diffusivity in the oxide scale was examined by using stable isotope oxygen ($^{18}O_2$). The oxidized alloy samples were annealed in $^{18}O_2$ (about 95 vol% of $^{18}O_2$, $p(^{18}O_2) = 0.1$ bar) at 1073 K for 300 s. After $^{16}O/^{18}O$ exchange, the ^{18}O concentration in the oxide scale was measured by secondary ion mass spectrometry (SIMS, Cameca, ims-5f) from oxide scale surface. The primary Cs^+ beam sputtered the sample surface in an area of 150 μm × 150 μm. The negative secondary ions ($^{16}O^-$, $^{18}O^-$, and some metal-oxide coupling ions) were detected as a function of sputtering times.

3. Results

3.1. Surface microstructures of oxidized Fe–Cr alloys

The surface microstructures of oxide scale were investigated by scanning electron microscopy (SEM). Fig. 1 shows SEM images of oxidized alloy surface at 1073 K for 72 h (at the initial oxidation stage). Both surfaces are composed of small oxide grains (each grain is less than 1 μm in width and length). In the case of Laves-phase forming alloy (Fig. 1(a)), no apparent grain boundaries of alloy are observed with relatively homogeneous oxide scale grains. On the other hand, oxidized SUS430 shows an increase of height at the grain boundaries of alloy (Fig. 1(b)). The rides formation on the oxide scale surface suggests that the preferential oxidation at the grain boundaries: this also suggests the higher diffusivity of elements at the alloy grain boundaries than at bulk. The EDX analysis indicated that the higher concentration of Mn, Fe, and Cr were observed at the alloy grain boundary parts. Thus, the oxidation of these elements is promoted at the alloy grain boundaries with a fast diffusion of elements, which affects the oxide scale growth rates. After long-term oxidation, the rides are not clear on the surface due to the thick oxide scale formation.

The oxide scale phases formed on the alloy surface were investigated by X-ray diffraction (XRD). Fig. 2 shows XRD patterns of oxidized alloy surfaces after oxidation at 1073 K for about 1100 h in H_2-H_2O. The identified phases were alloy (denoted as A), spinel-type oxides (denoted as S, such as $MnCr_2O_4$), and Cr_2O_3 type oxides (denoted as C). The peak intensities and peak position of these oxides are somewhat different between the examined alloys. This can be due to the concentration difference of spinel and Cr_2O_3 in the scale, and the difference of lattice parameters of spinel oxides associated from the composition change in $(Mn,Fe,Cr)_3O_4$. The precise analysis on the structural change will be examined in the future.

Table 1
Chemical composition of examined Fe–Cr alloys

	C	Al	Si	Cr	Mn	Fe	Ni	Nb	Mo	La
Laves-phase formed alloy	0.005	0.03	0.11	20.1	0.50	76.81	0.007	0.36	2.0	0.08
SUS430 alloy	0.048	–	0.35	18.31	0.21	81.10	–	–	–	–

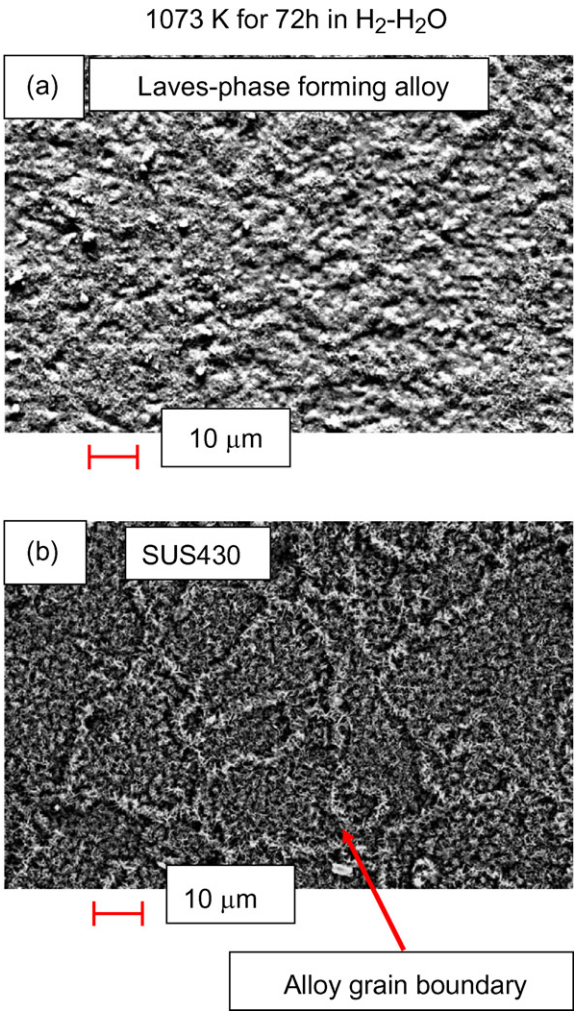

Fig. 1. Scanning electron microscope images of oxidized Fe–Cr alloys surface at 1073 K for 72 h in H_2-H_2O: (a) Laves-phase forming alloy and (b) SUS430.

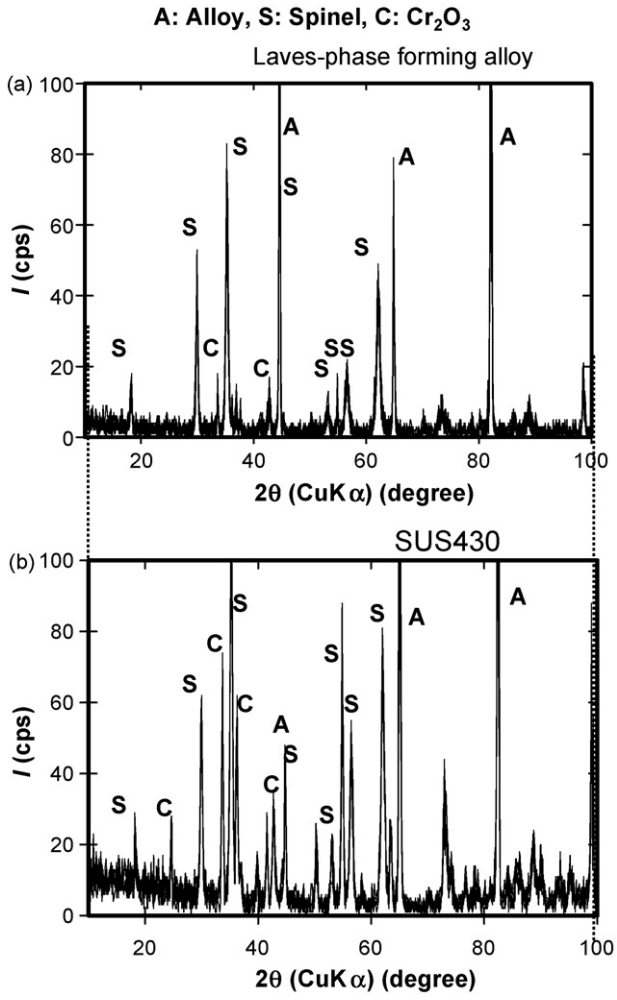

Fig. 2. X-ray diffraction patterns of oxidized alloys surface after oxidation at 1073 K for 1100 h in H_2-H_2O: (a) Laves-phase forming alloy and (b) SUS430.

3.2. Microstructures at oxide scale/alloy interfaces

Fig. 3 shows SEM images of oxide scale/alloy interfaces for two examined alloys after long-term oxidation: Laves-phase forming alloy (Fig. 3(a)) and SUS430 (Fig. 3(b)). In the Laves-phase forming alloy, the grain boundary of alloy is identified as white color lines. These lines are considered to be the Laves-phases (such as Fe_2Nb) precipitated from the alloy bulk. The oxide scale is identified as gray zone on top surface with a thickness about 2 μm. For SUS430 (Fig. 3(b)), there is no apparent precipitates at the alloy grain boundary. The oxide scale is identified as gray zone on the surface with a thickness of about 4 μm. The ridge parts are not clear in any cross-section because whole the alloys surface was covered with a thick oxide scales after long-term oxidation. The higher magnification image of oxide scale/alloy interface of Laves-phase forming alloy is presented in Fig. 3(c). The microstructure of oxide scale/alloy is compact without voids and cracks, suggesting a continuous growth of oxide scale from the alloy surface. The oxide scale is composed of plate-like or needle-like grains as observed in Fig. 1. The white grains observed at the oxide scale/alloy interfaces are the internal precipitates, such as Mo and Nb particles. Many gray spots are observed around the scale/alloy interfaces: these spots are considered to be Al_2O_3 internal oxides. The scale thickness is almost constant, and no difference of the Laves-phases was observed between beneath the oxide scales and the grain boundary part inside the alloy.

3.3. Elemental distributions at oxide scale/alloy interfaces

The elemental distributions were examined at the cross-sectional oxide scale/alloy interfaces for the Laves-phase forming alloy. Fig. 4 shows elemental distribution maps around oxide scale/alloy interfaces by EDX. The oxide scale is identified as high concentrations of Cr and Mn at the oxide scale part. Inside the alloy, relatively high concentrations of Mo and Nb are identified as lines. These are corresponding to the Laves-phases that are precipitated at the alloy grain boundary during heating. In some cases, the higher concentration of Mo and Nb are observed at the oxide scale/alloy interface as shown in Fig. 3(c). The formation of Laves-phase at the alloy grain boundary is relatively fast, and the diffusion of elements into oxide scale from alloy is controlled by the Laves-phase. The elemental distributions of depth direction are also examined by glow discharge

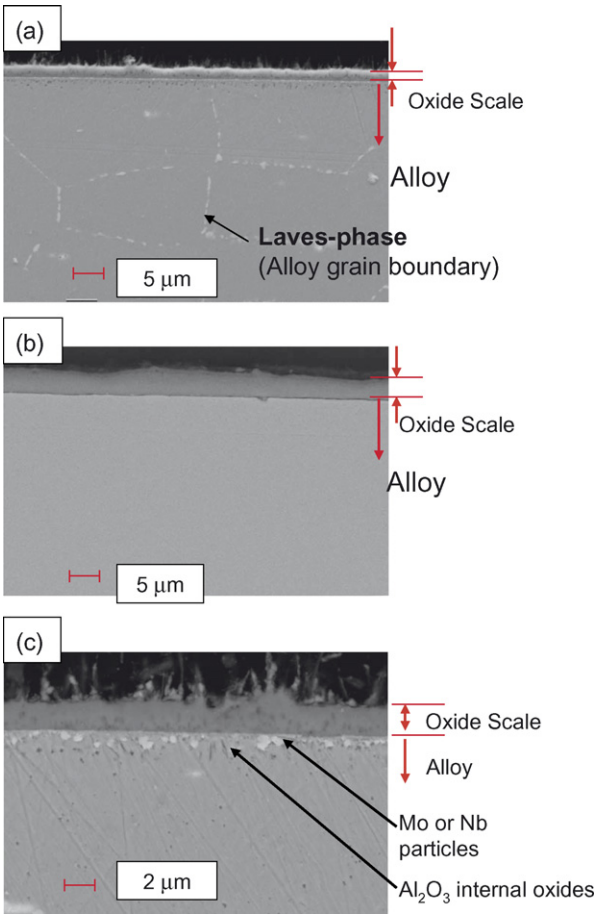

Fig. 3. Cross-sectional SEM image at oxide scale/alloy interfaces after oxidation at 1073 K for 1100 h in H_2-H_2O: (a) Laves-phase forming alloy, (b) SUS430, and (c) high magnification image of the Laves-phase forming alloy.

optical emission spectroscopy (GDOES). Fig. 5 shows GDOES depth profiles of oxidized alloys in an area of 2 mm in diameter. In this analysis, the depth profiles indicate the average intensities of each element around oxide scale/alloy interfaces. The *y*-axis indicates the optical intensity for each element, which is proportional to the concentration and sputtering rates (it is not the real concentration of each element). We assume the optical intensity for estimating the concentration of elements at a constant sputtering rate. For measurement of Mo, no data were recorded because no appropriate detector was equipped in this machine. The oxide scale is identified in the flat part of O-signal in the depth profiles. The oxide scale thickness is estimated from these profiles: the oxide scale thickness of Laves-phase forming alloy is only 2000 nm, while that of SUS430 is about 3500 nm. Thus, the thinner oxide scale thickness is accomplished in the Laves-phase forming alloys at the same annealing time. At the oxide scale surface, high signal counts of Cr and Mn are observed that corresponds to Cr–Mn spinel and Cr_2O_3. The Cr_2O_3-rich part is distributed close to the oxide scale/alloy interface. It should be noted that the concentration of Fe is low in the oxide scale surface for the Laves-phase forming alloy, while relatively high concentration at the oxide scale surface of SUS430. Around the oxide scale/alloy interface, the peak intensities of Si or Al are identified from the depth profiles: Al peak is distinct in the Laves-phase forming alloy (Fig. 5(a)), while Si peak is identified in the SUS430 (Fig. 5(b)). The GDOES peaks of Nb, Al, and Si are observed in the Laves-phase forming alloy (Fig. 5(b)): these peaks of elements are considered to be the internal oxides or precipitated grains at the oxide scale/alloy interfaces. Especially, Nb appears to be enriched at the oxide scale/alloy interfaces, which is corresponded to the white grain precipitates observed in Fig. 3(c). The signal intensity of Nb seems to be same level between inside the oxide scale and alloy: this can be due to low concentration of Nb in the alloy, although it concentrated at the grain boundary.

3.4. Kinetics of oxide scale growth

From GDOES depth profiles and SEM images, the oxide scale thickness was estimated at several annealing times. The oxide growth was compared between two different Fe–Cr alloys. Fig. 6 shows oxide scale thickness (x) as a function of annealing time (t). The square of oxide scale thickness is proportional to the annealing time in the following equation:

$$x_2 = k_p t \tag{1}$$

where x is the thickness of oxide scale, k_p is the parabolic growth rate constant, and t is the annealing time. The parabolic growth relationship suggests that the oxide scale growth is the diffusion controlled mechanism. From the slopes of the plots, the k_p values were calculated for the examined alloys: the obtained values are 4.5×10^{-14} cm^2 s^{-1} and 9.8×10^{-15} cm^2 s^{-1} for SUS430 and Laves-phase forming alloy, respectively. Therefore, a significant reduction of oxide scale growth rates is observed in the Laves-phase forming alloy.

3.5. Electrical conduction of oxidized alloys

The electrical conduction of oxidized alloys was examined in air by using AC impedance electrochemical method. Since the precise thickness of oxide scale was not measured for the measured samples, the area-specific resistance (ASR) was adopted as a conductivity of oxide scales:

$$\frac{1}{\mathrm{ASR}} = \frac{A}{T} \exp\left(\frac{E_a}{kT}\right) \tag{2}$$

where ASR (Ω cm^2) is the area-specific resistance, A is the constant, T (K) is the temperature, E_a (eV) is the activation energy for electronic conduction, and k is the Boltzman constant. Fig. 7 shows the temperature dependence of electrical conductivity for the oxidized alloys (oxidation at 1073 K for 600 h in H_2-H_2O). The 1/ASR values of both samples increases with an increase of temperature, suggesting the semi-conductor temperature dependence. Thus, the main contribution of electrical conductivity for this temperature dependence can come from the oxide scales on Fe–Cr alloys. The 1/ASR value of Laves-phase forming alloy shows the higher values than that of SUS430 at the same temperature. The area-specific resistances (ASR) are apparently different between two alloys: 69 mΩ cm^2 for the Laves-phase forming alloy, while 195 mΩ cm^2 for SUS430 at 973 K (the

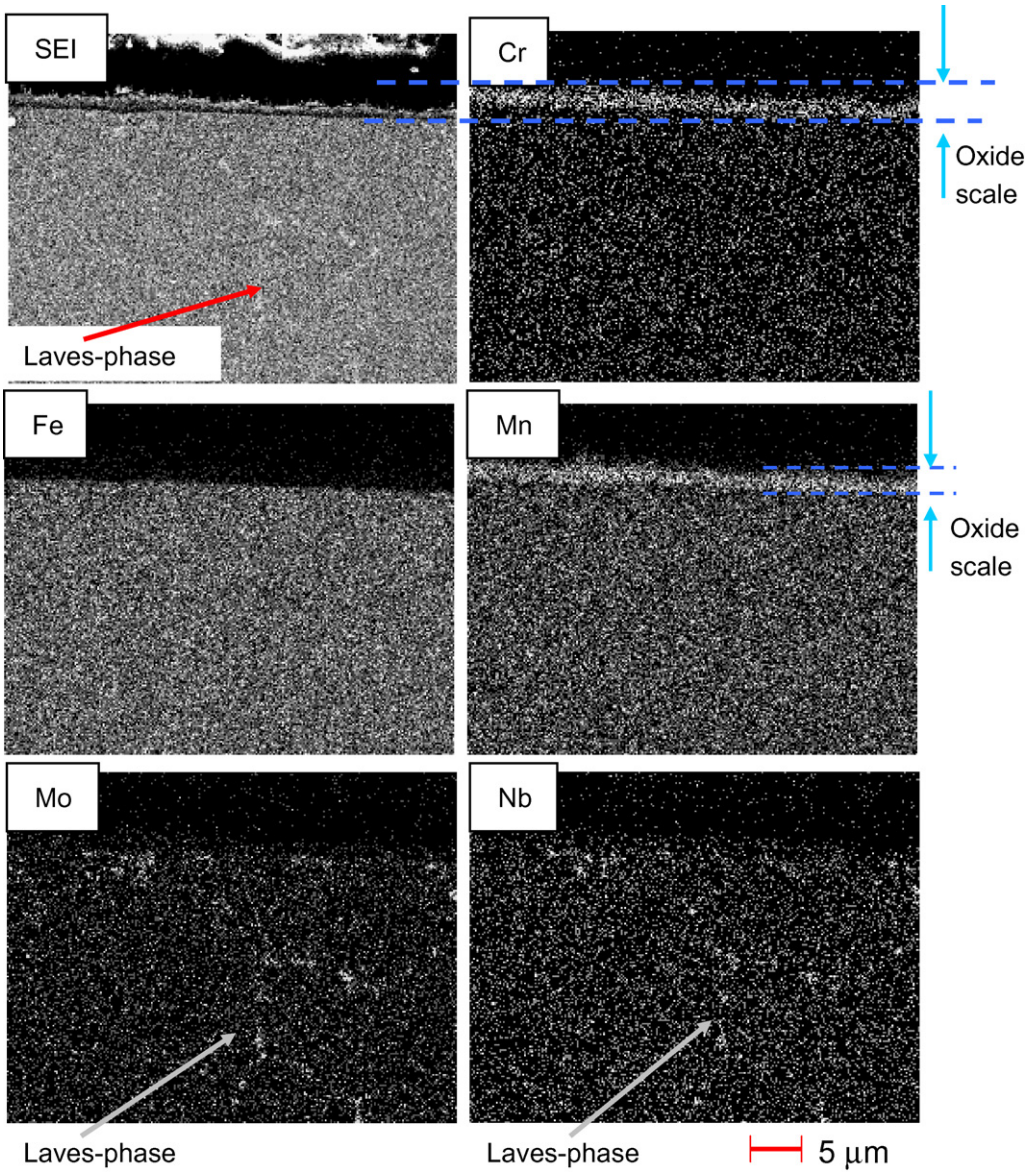

Fig. 4. Elemental distribution maps at oxide scale/alloy interfaces after oxidation at 1073 K for 1100 h in H_2-H_2O for Laves-phase forming alloy.

estimated thicknesses of oxide scale are 1.1 μm for the Laves-phase forming alloy and 3.2 μm for SUS430). The observed area-specific resistance of the Laves-phase forming alloy shows the lower values compared with the SUS430 and other Fe–Cr alloy. The activation energy of the Laves-phase forming alloy (0.37 eV) was lower than that of SUS430 (0.56 eV). The conduction mechanism and main contribution of oxide phase can be different between the Laves-phase forming alloy and SUS430 [14,15]. The oxidized Laves-phase forming alloy shows the better electrical conduction properties.

3.6. Oxygen diffusion in the oxide scales

In order to analyze the oxygen diffusivity in the oxide scale, isotope oxygen exchange ($^{16}O/^{18}O$ exchange) was conducted at 1073 K for 300 s for the oxidized samples. In this experimental condition, oxygen chemical potential was different between the gas/oxide scale interface and the oxide scale/alloy interfaces. Thus, the chemical diffusion of isotope oxygen ($^{18}O_2$) was evaluated from the diffusion profiles. Fig. 8 shows isotope oxygen diffusion profiles around the oxide scale/alloy interfaces. The isotope oxygen concentration ($C_{^{18}O}(x)$) at a depth of x was defined as the following equation:

$$C_{^{18}O}(x) = \frac{I_{^{18}O}(x)}{I_{^{16}O}(x) + I_{^{18}O}(x)} \quad (3)$$

where x, $I_{^{18}O}(x)$, and $I_{^{16}O}(x)$ indicate the depth from surface, signal counts of $^{16}O^-$, and signal counts of $^{18}O^-$, respectively. The oxide scale thickness was estimated to be about 2 μm and 3.8 μm for Laves-phase forming alloy and SUS430, respectively (after about 1100 h oxidation in H_2-H_2O atmosphere). The ^{18}O diffusion lengths are about 1.0 μm and 1.7 μm for the Laves-

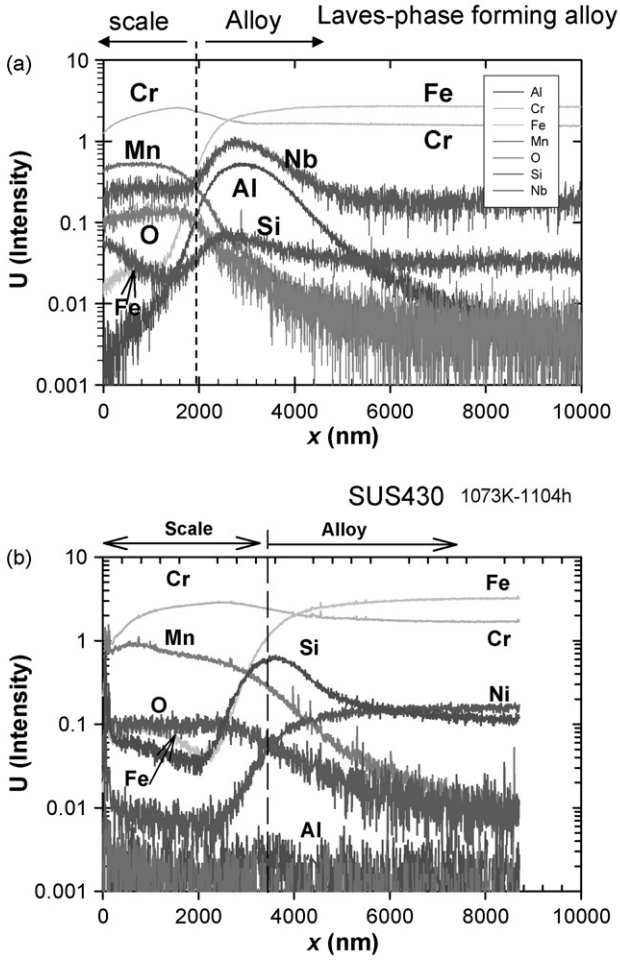

Fig. 5. Glow discharge optical emission spectroscopy (GDOES) depth profiles from oxide scale surface: (a) Laves-phase forming alloy and (b) SUS430.

phase forming alloy and SUS430, respectively. Thus, the ^{18}O diffusion is interrupted at about half part of oxide scales for both oxide scales. The solid lines are fitting lines from the appropriate equation (the solution for the Fick's second low) by Crank [16]

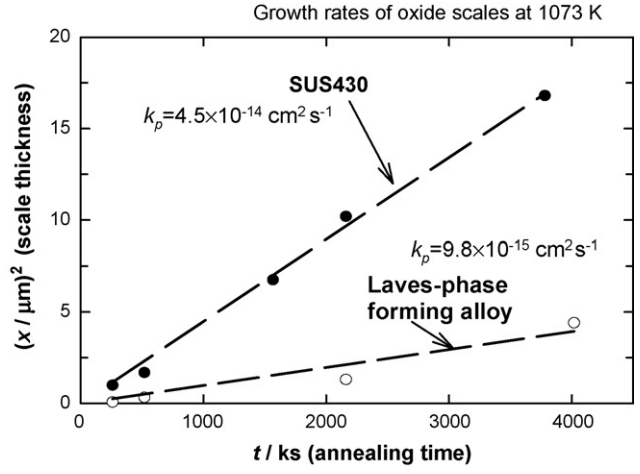

Fig. 6. Oxide scale thickness as a function of annealing time.

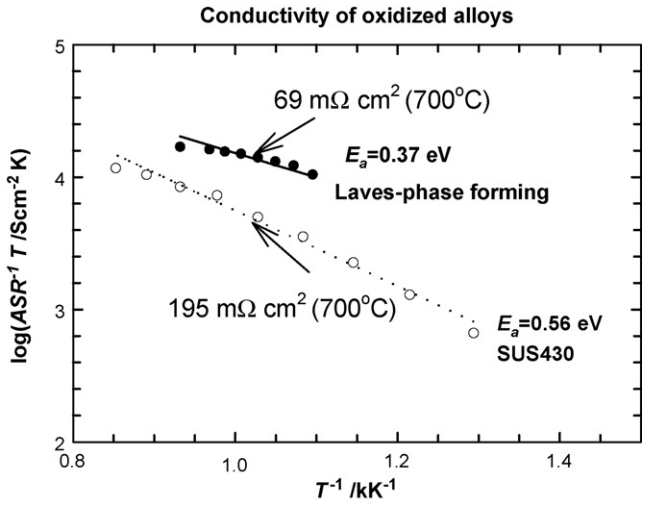

Fig. 7. Electrical conductivity (1/ASR values) of oxidized alloys as a function of inverse temperature.

assuming the surface reaction:

$$C_{^{18}O}(x) = (C_g - C_{bg})\left[\mathrm{erfc}\left(\frac{x}{2\sqrt{D^*t}}\right) - \exp(hx + h^2D^*t) \times \mathrm{erfc}\left(\frac{x}{2\sqrt{D^*t}} + h\sqrt{D^*t}\right)\right] + C_{bg} \quad (4)$$

where C_g is the concentration of ^{18}O in the gas phase, which is assumed to be constant during $^{16}O/^{18}O$ exchange ($C_g = 0.95$ for calculation), C_{bg} is the natural abundant level of ^{18}O ($C_{bg} = 0.002$), t is the annealing time for $^{16}O/^{18}O$ exchange (300 s), D^* is the chemical diffusion coefficient for isotope oxygen in the oxide scale. The parameter of h indicates the ratio of k and D^* ($h = k/D^*$, k is the surface reaction rate constant). The fitting lines to the observed data were not match with in the lower concentration range ($C_{^{18}O} \approx 0.001$–0.01). This is considered to be the contribution of grain boundary of oxide scale. The D^* value was calculated from the fitting of the above equation to the

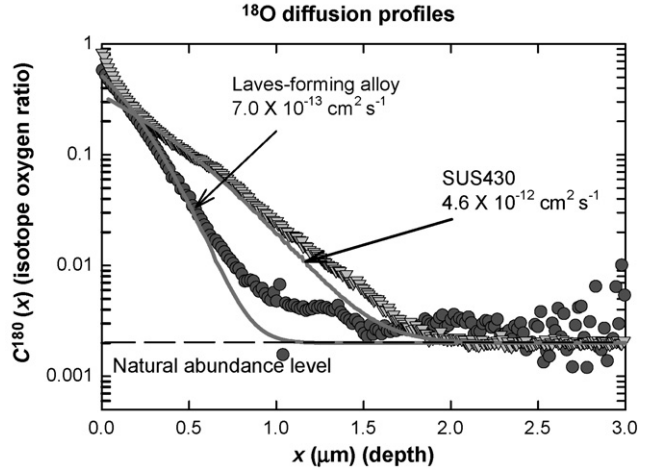

Fig. 8. Chemical diffusion profiles of ^{18}O in the oxide scales: (◯) diffusion profile of oxidized Laves-forming alloy and (▼) diffusion profile of oxidized SUS430.

measured data: $D^* = 7.0 \times 10^{-13}$ cm^2 s^{-1} for Laves-phase forming alloy and $D^* = 4.6 \times 10^{-12}$ cm^2 s^{-1} for SUS430. A decrease of D^* value was observed in the Laves-phase forming alloy. These values are about two orders of magnitude higher than those of oxide scale growth rates. Such high oxygen diffusivity suggests that oxygen inward diffusion at the top surface of oxide scale (it can be due to the Cr–Mn spinel phase or microstructures), and oxygen diffusivity inside the oxide scale can be different with position in the oxide scale.

4. Discussion

4.1. Oxide scale formation mechanism on Laves-phase forming alloy

At the initial stage of oxidation, ridges were formed at the alloy grain boundary of SUS430 whilst no apparent increase of height at the alloy grain boundary of Laves-phase forming alloys (Fig. 1). This suggests that elemental diffusion was decreased at the grain boundary of Laves-phase forming alloy (such as Mn and Fe diffusion). The oxide scale growth rate of the Laves-phase forming alloy was smaller than that of SUS430. The decrease of oxide scale growth rate has been discussed in many papers by considering small amounts of reactive elements (Zr, La, etc.) addition [1,2]. The examined SUS430 does not contain these reactive elements and this can increase the oxide scale growth rates. The oxide scale thickness in the Laves-phase forming alloy was less than 2 μm at 1073 K for more than 1000 h: this thickness is even thinner than the La-containing Fe–Cr alloy in the same experimental condition (observed scale thickness were about 3–4 μm). Therefore, the Laves-phase formation at the alloy grain boundary is considered to be one of the effective functions for lowering the oxide scale growth rates.

Both alloys showed the parabolic growth relationship, which suggests the diffusion-controlled mechanism for oxide scale growth (Fig. 6). The cation and oxygen diffusion through the oxide scale should be taken into account for the oxide scale growth mechanism. For cation diffusion through the scale (outward diffusion of cation), the diffusivity of cation is different from cation species and oxide scale phases. Fig. 9 shows schematic diagram of oxide scale growth and diffusion of elements in the oxide scales. The diffusivity of cations can be different in the main oxide scale phase formed on the surface: relatively high concentration of Fe was observed in the oxide scale of SUS430 while low concentration of Fe in the oxide scale of the Laves-phase forming alloys (Fig. 5). In the case of SUS430, the Cr-diffusion or Fe-diffusion in the spinel oxide ($(Fe,Cr,Mn)_3O_4$) can affect the scale growth rates due to the incomplete Cr_2O_3 layer by alloy grain boundary. On the other hand, Fe or Cr diffusion both in Cr–Mn spinel and Cr_2O_3-based oxides can control the formation of continuous and compact oxide scales on the Laves-phase forming alloy. The diffusivities of Fe in the Cr–Mn spinel ($(Fe, Cr,Mn)_3O_4$) are estimated to be far larger ($D_{Fe} \approx 10^{-13}$ cm^2 s^{-1}) than that of Fe in Cr_2O_3 ($D_{Fe} \approx 10^{-20}$ cm^2 s^{-1}) at $p(O_2) = 10^{-17}$ bar, 1073 K [14]. The

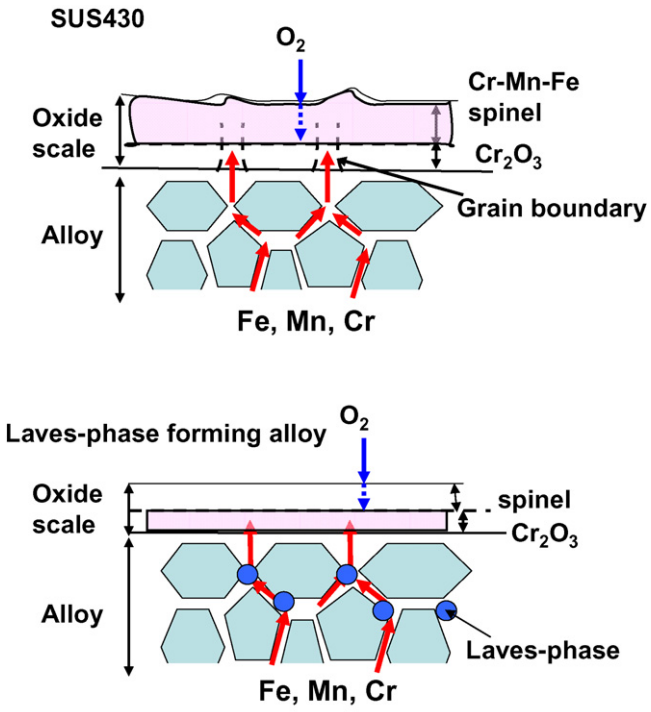

Fig. 9. Schematic diagram of oxide scale growth for two different Fe–Cr alloys: (a) SUS430 and (b) Laves-forming alloy.

temperature dependence of the 1/ASR value for the oxidized alloy also suggests the contribution of main oxide phase in the oxide scale: the lower activation energy of electrical conductivity at the Laves-phase forming alloy indicates the Cr_2O_3-based continuous scale affects the electrical conduction.

Extremely high oxygen diffusivity was observed for both oxidized alloys compared with the oxide scale growth rates (about two orders of magnitude difference). Thus, inward diffusion of oxygen should be taken into account for oxide scale growth. The diffusion length of oxygen is about 1.0 μm in the Laves-forming alloy in Fig. 8. This is about half length of oxide scale thickness of the Laves-forming alloy (thickness about 2.0 μm). Therefore, two oxide phases formation is considered inside the oxide scale; fast oxygen diffusion phase around the surface and low oxygen diffusion phase close to the scale/alloy interfaces. The surface fast diffusion phase is considered to be Cr–Mn spinel. The compositional change in the spinel oxide can affect the oxygen diffusivity (such as Fe concentration). We have also measured the oxygen diffusivity in the oxide scale for the other Fe–Cr alloys [10,17]. The observed chemical diffusion coefficients of ^{18}O in the oxide scale were in the order of magnitude 10^{-12} cm^2 s^{-1}, which is similar order of magnitude in this study. Thus, it seems that there is a fast ^{18}O diffusion layer in the oxide scale surface even in the other oxide scales on Fe–Cr alloys. In the previous reports [18], the hydroxide species can also diffuse into the oxide scales. Thus, the effect of hydroxide should be considered for the oxygen diffusion in the oxide scale. In any case, the inward diffusion of oxygen and the outward diffusion of cation through the oxide scale should be taken into account for oxide scale growth. The more precise analysis will be reported in the near future.

4.2. Electrical conduction of oxidized alloys

As introduced above, the activation energy of electrical conduction (1/ASR value) for the oxidized sample was lower in the Laves-phase forming alloy than that in SUS430 (Fig. 7). This indicates the difference of the electrical conduction mechanism. From the previous reports [15], the activation energy for electrical conductivity of Cr_2O_3 on Cr-metal is around 0.44 eV, which is similar value with that of oxide scales on the Laves-phase forming alloy. The activation energy for electrical conduction of Cr–Mn spinel on Fe–Cr alloy was reported to be 0.89 eV, which is higher than that of Cr_2O_3 [17]. Therefore, the temperature dependence of electrical conduction can come from the Cr_2O_3-based oxide in the oxide scale in the case of Laves-phase forming alloy. An increase of the 1/ASR value and decrease of the activation energy in the Laves-forming alloy is attributed to the thinner oxide scale thickness and continuous Cr_2O_3-based oxide scale formation around the oxide scale/alloy interfaces.

4.3. Application of Laves-phase forming alloys to SOFC interconnects

The present results suggest that the Laves-phase forming alloy is suitable for SOFC interconnects in terms of oxidation resistance and electrical conduction in H_2-H_2O. The thickness of oxide scale was less than half of SUS430 with compact and clean oxide scale/alloy interfaces. One point that should be clarified is the mechanical strength of oxidized alloys. The formation of Laves-phase at the alloy grain boundary is effective for oxidation. However, a deteriorate effect is assumed in the mechanical strength due to the Laves-phase formation. In the near future, we will examine this issue to clarify the applicability of this alloy. A similar alloy has already been tested in the real SOFC stacks as interconnects by Versa Power Systems [19]. So far, a positive result was reported in terms of long-term stability, and this alloy is one promising metallic interconnects for SOFCs.

5. Conclusion

The oxide scale formation mechanism was investigated in the Laves-phase forming alloy in H_2-H_2O at 1073 K for the SOFC interconnects. The oxide scale growth rates were reduced in the Laves-phase forming alloy compared with the typical stainless steel, SUS430. One of the effective functions for the reduction of oxide scale growth is the precipitation of the Laves-phases at the alloy grain boundary. The area-specific resistance (ASR) of oxidized Laves-phase forming alloy showed the lower values than that of SUS430. The temperature dependence of 1/ASR value for oxidized alloy was different between Laves-phase forming alloy and SUS430; Laves-phase forming alloy shows similar activation energy with Cr_2O_3. The oxygen diffusivity in the oxide scale was evaluated by the stable isotope oxygen ($^{18}O_2$) diffusion in the scale. The chemical diffusion coefficients of isotope oxygen in the oxide scale were as follows: $D = 7.0 \times 10^{-13}\ cm^2\ s^{-1}$ for Laves-phase forming alloy and $D = 4.6 \times 10^{-12}\ cm^2\ s^{-1}$ for the SUS430. A relatively high diffusivity of oxygen was estimated in the Mn–Cr spinel oxide on the top surface of oxide scales. Inward diffusion of oxygen and outward diffusion of cation in the oxide scale were discussed to consider the oxide scale growth mechanism. When considering the application for SOFC interconnects, the Laves-phase forming alloy possesses a high potential in terms of oxidation resistance and electrical conductivity.

Acknowledgement

The Laves-phase forming alloy samples were kindly supplied from Dr. Ishikawa (JFE Steel Corporation, Japan). The authors thank the cooperation.

References

[1] H.U. Anderson, F. Tietz, in: S.C. Singhal, K. Kendall (Eds.), Interconnects in High Temperature Solid Oxide Fuel Cells, Elsevier, 2003, chapter 7.
[2] J.W. Fergus, Mater. Sci. Eng. A 397 (2005) 271.
[3] W.J. Quadakkers, T. Malkow, J. Piron-Abellan, U. Flesch, V. Schemet, L. Singheiser, in: A.J. McEvoy (Ed.), Proceedings of Fourth European SOFC Forum, The European SOFC Forum, Switzerland, 2000, p. 827.
[4] K. Huang, P.Y. Hou, J.B. Goodenough, Solid State Ionics 129 (2000) 237.
[5] T. Uehara, A. Toji, K. Inoue, M. Yamaguchi, T. Ohno, in: S.C. Singhal, M. Dokiya (Eds.), In Solid Oxide Fuel Cells VIII, PV2003-07, The Electrochemical Society Inc., Pennington, USA, 2003, p. 914.
[6] Z. Yang, J.S. Hardy, M.S. Walker, G. Xia, S.P. Simner, J.W. Stevenson, J. Electrochem. Soc. 151 (2004) A1825.
[7] A. Toji, T. Uehara, Extended Abstract of 14th SOFC Symposium, The SOFC Society of Japan, Tokyo, 2005, p. 60.
[8] T. Horita, Y. Xiong, K. Yamaji, N. Sakai, H. Yokokawa, J. Electrochem. Soc. 150 (3) (2003) A243.
[9] T. Horita, Y. Xiong, H. Kishimoto, K. Yamaji, N. Sakai, H. Yokokawa, J. Power Sources 118 (2003) 35–43.
[10] T. Horita, K. Yamaji, Y. Xiong, H. Kishimoto, N. Sakai, H. Yokokawa, J. Power Sources 131 (2004) 293.
[11] S. Ide, Y. Funakawa, Y. Kato, O. Furukimi, Materia Japan 45 (2) (2006) 135.
[12] S. Ishikawa, S. Ide, Y. Kato, O. Furukimi, Proceedings of the 14th Sympoium on Solid Oxide Fuel Cells in Japan Extended Abstract, 2005, p. 146.
[13] S. Ishikawa, S. Ide, Y. Kato, T. Ujiro, Proceedings of the 15th Sympoium on Solid Oxide Fuel Cells in Japan Extended Abstract, 2006, p. 136.
[14] R. Dieckman, J. Phys. Chem. Solids 59 (4) (1998) 507.
[15] J.-H. Park, K. Natesan, Oxid. Met. 33 (1990) 31.
[16] J. Crank, The Mathematics of Diffusion, 2nd ed., Oxford University Press, Oxford, 1975.
[17] N. Sakai, T. Horita, Y.P. Xiong, K. Yamaji, H. Kishimoto, M.E. Brito, H. Yokokawa, T. Maruyama, Solid State Ionics 176 (2005) 681.
[18] Z. Yang, M.S. Walker, P. Singh, J.W. Stevenson, T. Norby, J. Electrochem. Soc. 151 (2004) B669.
[19] S. Benhaddad, J. Protkova, W. Dueck, S. Sherman, Solid Oxide Fuel Cells 10, in: K. Eguchi, S.C. Singhal, H. Yokokawa, J. Mizusaki (Eds.), ECS Transactions, 7 (1) (2007) 2125.